







Article

Magnetoelectric Properties of Aurivillius-Layered Perovskites

Vadla Veenachary ¹, Eskilla Venkata Ramana ^{2,*}, Simhachalam Narendra Babu ¹, Venkata Sreenivas Puli ³, Sujoy Saha ⁴, Gopalan Srinivasan ⁴, G. Prasad ¹ and N. V. Prasad ^{1,*}

¹ Materials Research Laboratory, Department of Physics, Osmania University, Hyderabad 500013, India; veenachary1@gmail.com (V.V.); narendraphysics@gmail.com (S.N.B.); gudurup@osmania.ac.in (G.P.)

² I3N-Aveiro, Department of Physics, University of Aveiro, 3810 193 Aveiro, Portugal

³ Smart Nanomaterials Solutions, Orlando, FL 32707, USA; pvsri123@gmail.com

⁴ Physics Department, Oakland University, Rochester, MI 48307, USA; sahasujoy3@gmail.com (S.S.); srinivas@oakland.edu (G.S.)

* Correspondence: ramana.venkata@ua.pt (E.V.R.); nvp1969@rediffmail.com (N.V.P.)

Abstract: In the present work, we have synthesized rare-earth ion modified $\text{Bi}_{4-x}\text{RE}_x\text{Ti}_2\text{Fe}_{0.7}\text{Co}_{0.3}\text{O}_{12-\delta}$ (RE = Dy, Sm, La) multiferroic compounds by the conventional solid-state route. Analysis of X-ray diffraction by Rietveld refinement confirmed the formation of a polycrystalline orthorhombic phase. The morphological features revealed a non-uniform, randomly oriented, plate-like grain structure. The peaks evident in the Raman spectra closely corresponded to those of orthorhombic Aurivillius phases. Dielectric studies and impedance measurements were carried out. Asymmetric complex impedance spectra suggested the relaxation of charge carriers belonging to the non-Debye type and controlled by a thermally activated process. Temperature-dependent AC conductivity data showed a change of slope in the vicinity of the phase transition temperature of both magnetic and electrical coupling natures. Based on the universal law and its exponent nature, one can suppose that the conduction process is governed by a small polaron hopping mechanism but significant distortion of TiO_6 octahedral. The doping of the A-sites with rare-earth element ions and changes in the concentrations of Fe and Co ions located on the B-sites manifested themselves in saturated magnetic hysteresis loops, indicating competitive interactions between ferroelectric and canted antiferromagnetic spins. The magnetic order in the samples is attributed to pair-wise interactions between adjacent $\text{Fe}^{3+}-\text{O}-\text{Fe}^{3+}$, $\text{Co}^{2+/3+}-\text{O}-\text{Co}^{3+/2+}$, and $\text{Co}^{2+/3+}-\text{O}-\text{Fe}^{3+}$ ions or Dzyaloshinskii–Moriya interactions among magnetic ions in the adjacent sub-lattices. As a result, enhanced magnetoelectric coefficients of 42.4 mV/cm-Oe, 30.3 mV/cm-Oe, and 21.6 mV/cm-Oe for $\text{Bi}_{4-x}\text{Dy}_x\text{Ti}_2\text{Fe}_{0.7}\text{Co}_{0.3}\text{O}_{12-\delta}$ (DBTFC), $\text{Bi}_{4-x}\text{La}_x\text{Ti}_2\text{Fe}_{0.7}\text{Co}_{0.3}\text{O}_{12-\delta}$ (LBTFC), and $\text{Bi}_{4-x}\text{Sm}_x\text{Ti}_2\text{Fe}_{0.7}\text{Co}_{0.3}\text{O}_{12-\delta}$ (SBTFC), respectively, have been obtained at lower magnetic fields (<3 kOe). The strong coupling of the Aurivillius compounds observed in this study is beneficial to future multiferroic applications.

Keywords: multiferroic; Aurivillius; impedance spectra; magnetoelectric; dielectric studies; magnetic studies; structural studies



Citation: Veenachary, V.; Ramana, E.V.; Narendra Babu, S.; Puli, V.S.; Saha, S.; Srinivasan, G.; Prasad, G.; Prasad, N.V. Magnetoelectric Properties of Aurivillius-Layered Perovskites. *Crystals* **2024**, *14*, 299. <https://doi.org/10.3390/cryst14040299>

Academic Editor: Zhonghua Yao

Received: 18 February 2024

Revised: 10 March 2024

Accepted: 18 March 2024

Published: 22 March 2024



Copyright: © 2024 by the authors. Licensee MDPI, Basel, Switzerland. This article is an open access article distributed under the terms and conditions of the Creative Commons Attribution (CC BY) license (<https://creativecommons.org/licenses/by/4.0/>).

1. Introduction

Multiferroic compounds are a fascinating type of material that have garnered remarkable attention in the realm of materials science. Multiferroics exhibit two or more orders of ferroelectric (FE), ferroelastic, and magnetic (ferromagnetism (FM)/anti-ferromagnetism (AFM)) orders in the single phase. The present Aurivillius phase materials have shown their potential usage in many novel applications, like memory storage devices, sensors, transducers, and actuators [1]. Multiferroics are promising materials due to their potential applications that exploit the combination of ferroelectric and magnetic orders [1,2]. The most fascinating prospect of research on these materials is tuning the electric dipoles by applying magnetic fields under superimposed small AC magnetic fields [3–7]. The coupling between ferroelectric (FE) and ferromagnetic (FM) orders makes it easier and

faster to address a data bit in memory devices [2,8]. This could lead to the development of magnetoelectric materials owing to their speed in read/write operations. However, very few room-temperature magnetoelectric (ME) compounds have been reported, due to the mutual exclusion nature of FM and FE in single-phase compounds. Ferroelectricity is attributed to empty d-orbitals, while partially or half-filled d-orbitals are responsible for magnetic nature [9]. In the path of searching for single-phase multiferroic compounds, Aurivillius phase multiferroics are a class of bismuth layer compound that have been extensively investigated for their flexibility and the tunable nature of their ferroelectric and magnetic properties [10–17].

The general formula of Aurivillius phase compounds can be expressed as $(\text{Bi}_2\text{O}_2)^{2+}(\text{A}_{m-1}\text{B}_m\text{O}_{3n+1})^{2-}$, where m represents the dimensionality of perovskites $(\text{A}_{m-1}\text{B}_m\text{O}_{3n+1})$, which are sandwiched between fluorite-like $(\text{Bi}_2\text{O}_2)^{2+}$ layers. Here, A is the cuboctahedral site, which can be substituted by mono-, di-, or tri-valent elements and B is the octahedral site (BO_6), which can be substituted by di-, tri-, tetra-, or pentavalent elements [18]. The Aurivillius phase compounds were found to be familiar for their ferroelectric/magnetoelectric behavior, high transition temperatures, and strong anisotropic nature of spontaneous polarization [19]. Rare earth-modified A-site Aurivillius phases were studied to explore the changes in structural and ferroelectric properties [20]. These materials are well-suited for non-volatile memory devices due to their fatigue-free nature. Recently, many Aurivillius phase compounds have shown room temperature magnetoelectric output when Fe/Co/Ni were placed in the B-sites. However, the origin of the combined ferroelectric and magnetic and its coupling are still under discussion. Therefore, a strategic way is required in choosing magnetic ions, which triggers the enhanced magnetoelectric output in the materials. It is a known fact that the multiferroic properties can be altered by the concentration of magnetic ions in the B-sites. From previous literature, iron-doped Aurivillius phase compounds show strong multiferroic behavior at room temperature [12,21]. These materials can be expressed as $\text{Bi}_{m+1}\text{Fe}_{m-3}\text{Ti}_3\text{O}_{3m+3}$ (BFTO- m). More interestingly, the key factors of the Aurivillius phase materials are that: (i) the origin of ferroelectricity is a combination of oxygen octahedral rotation and polar distortion; (ii) different numbers of layers in perovskite plates show significant differences in physical and structural properties.

In the last decade, much research has been focused on different layered compounds, such as $\text{Bi}_5\text{FeTi}_3\text{O}_{15}$, $\text{Bi}_6\text{Fe}_2\text{Ti}_3\text{O}_{18}$, $\text{Bi}_7\text{Fe}_3\text{Ti}_3\text{O}_{21}$, etc. [22–28]. The reported study on the Aurivillius family embodies two main aspects: (i) aliovalent doping at A- and B-sites to enhance the multiferroic performance, and (ii) processing mediated structure-property correlations in ceramics, thin films, single crystals, and intergrowths [29–36].

The three-layer structure of bismuth titanate ($\text{Bi}_4\text{Ti}_3\text{O}_{12}$ —BIT) has attracted researchers due to its high ferroelectric transition temperature (above 600 °C), low processing temperature compared to higher-layer structured compounds, and its anisotropic ferroelectric behavior [37–41]. However, these compounds possess high conductivity due to the volatile nature of bismuth at higher temperatures. This results in leakage currents, which deteriorate the ferroelectric nature [42–45]. The incorporation of rare-earth ions at the A-site has been demonstrated as an effective approach to mitigate this trade-off [13,46,47]. A noteworthy observation by Lu et al. is that Fe-doped BIT ceramics exhibit weak room-temperature ferromagnetic behavior [48]. Shigyo et al. reported that the La-, Nd-, and Sm-doped BIT samples show improved magnetic and ferroelectric properties due to controlled oxygen vacancies [49]. According to Paul et al., $\text{Bi}_{4-x}\text{Sm}_x\text{Ti}_{3-x}\text{Co}_x\text{O}_{12-\delta}$ at $x = 0.07$ has shown that the coefficient of ME coupling is about 0.65 mVcm^{-1} [50]. In recent studies, Yu et al. have reported an ME coefficient of $31.58 \text{ mVcm}^{-1}\text{Oe}^{-1}$ for $\text{Bi}_4\text{LaTi}_3\text{Co}_{0.3}\text{Fe}_{0.7}\text{O}_{15}$ ceramics [51]. Aurivillius phases possessing antiferromagnetic order or weak ferromagnetic order have limitations for their practical use [52–54]. These defects can be controlled by RE ions for the A-sites of Aurivillius phases. It should be remembered that the stoichiometry and synthesis conditions play a vital role in optimizing the ME coupling.

The major endeavor of the present work was to diminish the leakage current by introducing RE ions in the A-sites of perovskites and enhancing the cross coupling. We prepared

RE (Dy, Sm, La) ion-doped $\text{Bi}_4\text{Ti}_2\text{Fe}_{0.7}\text{Co}_{0.3}\text{O}_{12-\delta}$ ceramics. Electrical, magnetic, and ME measurements were carried out. The dispersion in AC-conductivity and relaxations in the low-frequency range above 200 °C were explained in terms of Maxwell–Wagner and multiple relaxations (non-Debye type). The presence of a small polaron conduction mechanism played a vital role. The dielectric relaxations observed near 200 °C can be attributed to the charge hopping of Ti^{3+} to $\text{Ti}^{4+}/\text{Fe}^{2+}$ to Fe^{3+} ions. The low concentration doping of lanthanides enhanced the dielectric properties. Apart from the above aspects, understanding structural evolution is interesting in Aurivillius phase compounds. Systematic studies on X-ray, Raman, and impedance analysis confirm the inherited magnetoelectric properties. Remarkably, the Dy-doped $\text{Bi}_4\text{Ti}_2\text{Fe}_{0.7}\text{Co}_{0.3}\text{O}_{12-\delta}$ (DBTFC) sample showed an ME coefficient of ~ 42.4 mV/cm-Oe at room temperature. Such systematic studies have not been reported so far.

2. Materials and Methods

Aurivillius multiferroic ceramics $\text{Bi}_{4-x}\text{RE}_x\text{Ti}_2\text{Fe}_{0.7}\text{Co}_{0.3}\text{O}_{12-\delta}$ (RE = Dy, Sm, La) were synthesized by conventional solid-state reaction method. For this purpose, stoichiometric amounts of reagents (purity > 99.9%) Bi_2O_3 , Sm_2O_3 , Dy_2O_3 , La_2O_3 , TiO_2 , Fe_2O_3 , and Co_3O_4 were milled in a planetary mill for 24 h using zirconia balls followed by calcination at 850 °C for 4 h. The calcined powder was again grounded with an agate mortar and pestle. The powder mixed with 2 wt.% polyvinyl alcohol binder was pressed into circular pellets with a thickness of around 1 mm and a diameter of 10 mm by a uniaxial hydraulic press. The green pellets were sintered at 900 °C for 4 h to attain higher density. The RE (Dy, Sm, and La) ion-doped $\text{Bi}_4\text{Ti}_2\text{Fe}_{0.7}\text{Co}_{0.3}\text{O}_{12-\delta}$ compounds were named DBTFC, SBTFC, and LBTFC, respectively.

Phase conformation of all the samples was performed by Powder X-ray diffraction using a PAN analytic X'Pert diffractometer (Almelo, The Netherlands). The sintered discs were crushed into powders and annealed at 400 °C to relieve mechanical strain. Rietveld refinement was also performed for all samples using Full-Prof Suit software (Version 3). The phase of all samples was well matched with standard three-layered compounds of XRD data (BIT, ICDD#00-008-0258). To study surface morphology and elemental analysis (Energy Dispersive X-ray spectroscopy, EDAX) the samples were analyzed using a ZEISS-EVO185 SEM instrument (Oberkochen, Germany). Image J 1.54h software was used to calculate the average grain size of the sintered pellets, employing histograms with Gaussian distribution. Raman spectra were measured using a Jobin Yvon spectrometer (Horiba, Japan) with a 532 nm excitation laser. The magnetization–magnetic field measurements were carried out using a vibrating sample magnetometer (VSM, Cryogenic, London, UK). ME studies were performed using a micro-measurement Group Strain Indicator, Model 3800, and a series WK strain gauge. The samples were electrically and magnetically poled before ME was performed. Ferroelectric characterization was carried out by measuring polarization–electric field hysteresis loops under various drive voltages using a custom-made loop tracer. Before electrical measurements, the samples were poled under an electric field of 20 kV/cm by placing them in a silicon oil bath at 120 °C and cooling them in the presence of the field. Magnetic poling was performed by placing the samples in the magnetic field at 5 kOe at room temperature (RT).

3. Results and Discussion

3.1. Powder X-ray Diffraction and Morphological Studies

The powder X-ray diffraction patterns of DBTFC, SBTFC, and LBTFC were obtained in the range of 20–80° at room temperature. The diffraction peaks of the compounds were in good agreement with the standard XRD pattern of $\text{Bi}_4\text{Ti}_3\text{O}_{12}$ (ICDD#00-008-0258) with space group $Fm\bar{3}m$ as shown in Figure 1a–c [55,56]. The XRD data were fitted into Rietveld refinement with Full-Prof software (version 3). The refining analysis revealed that all samples consisted mainly of a single-phase structure with an admixture of another phase of $\text{Bi}_{12}\text{Fe}_{0.5}\text{Ti}_{0.5}\text{O}_{20}$ belonging to the $I23$ space group. From the XRD studies, it could be

concluded that the pyrochlore ($\text{Bi}_{12}\text{FeO}_{20}$) formation was mainly due to the substitution of heterovalent elements (Ti^{4+} , Fe^{3+} , and Co^{2+}) in the B-site of the ABO_3 perovskites of the Aurivillius phases [55,57]. The reliability parameters (R_p , R_{wp} , and R_{exp}) and goodness of fit (χ^2) were within the specified range and well-matched between theoretical and experimental diffraction patterns. The experimental and theoretical values of reliability (R) factors revealed the quality of the phase formation of compounds and the observed error was found to be less than 15% for higher present structured phases [58]. Here, the pseudo-Voigt function was adopted to refine the XRD patterns (the original curve is a combination of both Gaussian and Lorentzian).

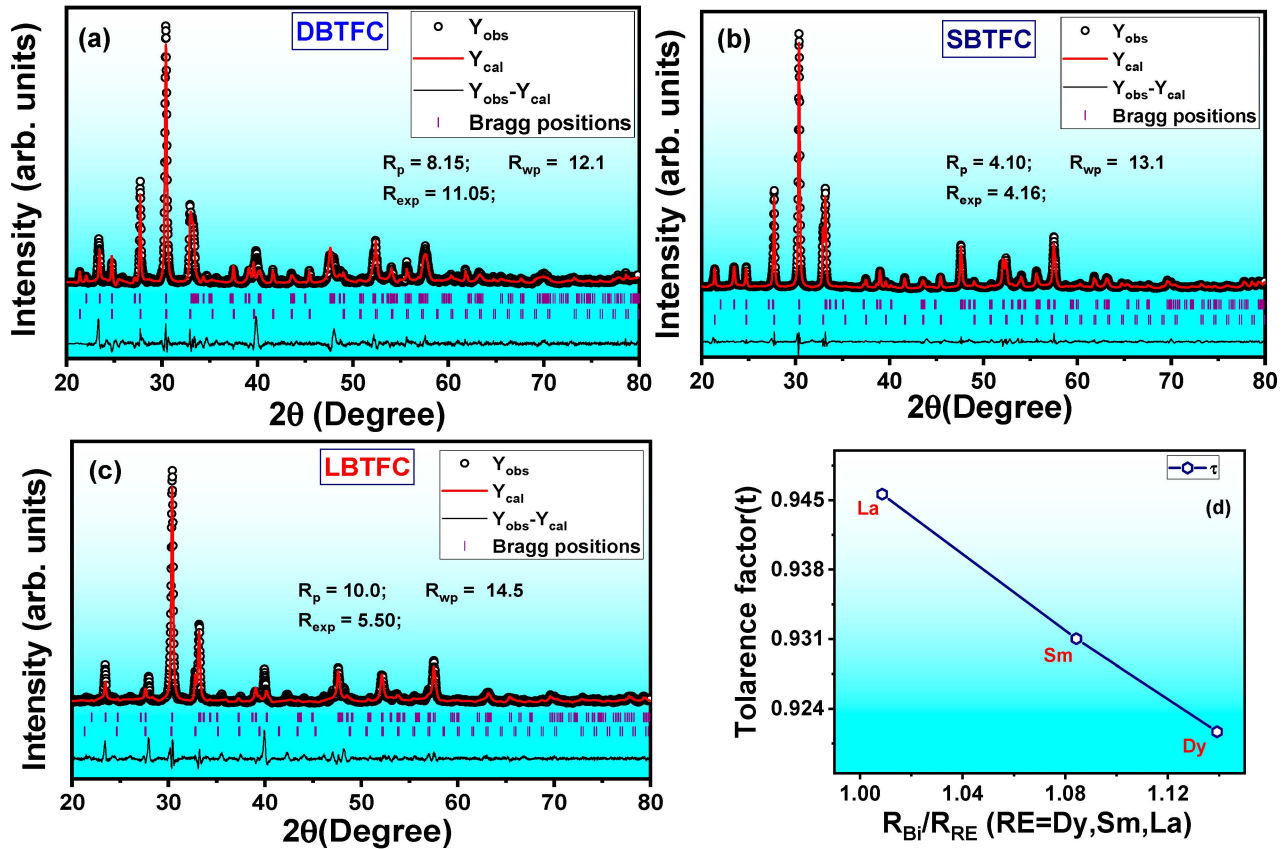


Figure 1. (a–c) Rietveld refinement of XRD patterns of the DBTFC, SBTFC, and LBTFC ceramics; (d) tolerance factor τ vs. R_{Bi}/R_{RE} .

The tolerance factor (τ) explains the perovskite nature of the samples. It is reported that $\tau < 1$ indicates perovskite nature. From these values, one can understand the tilt of TiO_6 octahedral, which is mainly responsible for dielectric relaxations in the layered perovskite compounds. The tolerance factor for the present compounds was calculated using the following equation [59,60]:

$$\tau = \frac{R_A + R_O}{\sqrt{2} (R_B + R_O)} \quad (1)$$

The terms R_A , R_B , and R_O represent the ionic radii of A-site, B-site, and Oxygen ions respectively. The variation of the tolerance factor with the ratio of R_{Bi}/R_{RE} is shown in Figure 1d. The size of the RE ionic radii is smaller than the Bi^{3+} (1.35 \AA) and follows Hume–Rothery conditions [59], and therefore it is reasonable to infer that RE ions can readily be substituted with Bi^{3+} sites [60]. The changes observed in the tolerance factor are due to A–O and B–O bond lengths, which would be reflected in the octahedral tilt. More aspects of this are seen in the Raman spectra, near 800 cm^{-1} which corresponds to

the stretching of TiO_6 . The lattice parameters (a , b , c), volumes are given in Table 1 and structural parameters are given in Table 2. The most intense peak was observed around 30° and indexed as (117). The intensity of the peak associated with the (117) plane of $\text{Bi}_4\text{Ti}_3\text{O}_{12}$ was highest, indicating that the prepared ceramic composition conformed to the three-layered structure ($m = 3$). The result is consistent with common reporting of the strongest diffraction reflection, corresponding to (1, 1, $2m + 1$) reflection in the Aurivillius phase three-layered compound [56].

Table 1. Lattice and Rietveld refinement parameters of DBTFC, SBTFC, and LBTFC.

Sample Name	DBTFC		SBTFC		LBTFC	
Space group	<i>Fmmm</i>	<i>I23</i>	<i>Fmmm</i>	<i>I23</i>	<i>Fmmm</i>	<i>I23</i>
Lattice parameters (Å)	a = 5.415 b = 5.381 c = 32.231	a = 10.173	a = 5.401 b = 5.400 c = 32.331	a = 10.175	a = 5.401 b = 5.399 c = 32.291	a = 10.220
Volume fraction (%)	82.300	17.700	79.78	20.22	99.70	0.300
Reliability factors (%)	$R_p = 8.15$; $R_{wp} = 12.10$; $R_{exp} = 11.05$		$R_p = 4.10$; $R_{wp} = 13.10$; $R_{exp} = 4.16$		$R_p = 10.01$; $R_{wp} = 14.50$; $R_{exp} = 5.50$	
Goodness of fit (χ^2)	5.88		9.95		6.90	

Table 2. Structural parameters of DBTFC, SBTFC, and LBTFC.

Sample Name	DBTFC	SBTFC	LBTFC
Orthorhombic Distortion (b/a)	0.993	0.9998	0.9996
Tetragonal strain (c/a)	5.9521	5.9861	5.9787
Orthorhombicity ($2(a - b)/(a + b) \times 10^2$)	0.629	0.018	0.003

3.2. Morphological Studies

The morphological images of the prepared ceramics were carried out by FESEM (field emission scanning electron microscope) as shown in Figure 2. Randomly oriented plate-like grains were observed in all ceramics. This kind of surface morphology is a characteristic of Aurivillius phase ceramics [60]. It was also observed that all grains were non-uniform and closely packed. The experimental densities of pellets were found to be roughly 98%. Based on the mentioned values, the samples were found to be denser. The histograms of grain sizes were drawn and well-fitted by the Gaussian distribution function as shown in the inset of Figure 2. The mean grain sizes of the pellets were observed to be ~ 0.492 , 0.490 , and $0.496 \mu\text{m}$ for DBTFC, SBTFC, and LBTFC, respectively.

Furthermore, grains associated with impurity phases were found in all samples, circled in the SEM pictures in Figure 2. The presence of an additional magnetic phase was obvious due to heterovalent element substitution in the B-sites of perovskites [61]. EDAX (energy dispersive X-ray analysis) studies were performed on all samples to calculate the elemental composition. The experimental (measured) and theoretical (estimated) percentage of elements are presented in the inserted table of Figure 3a–c. The measured atomic percentages of the elements were consistent with the expected formula. Based on the SEM photographs, one can speculate the formation of pyrochlore or secondary phase or mixture of $\text{Fe}^{2+}/\text{Co}^{2+}$ (marked as red circle in Figure 2). Similar results were more pronounced in the intergrowth Aurivillius phase compounds [62,63]. It was also observed that grain size and uniformity were found to be greater in LBTFC. The appearance of lamellar morphology along with the micro-pores could not be executed, which indicated a low density ($>97\%$) of the sample. As a result, the element composition in all samples was found to be closer to the expected values, and it can be concluded that Fe^{3+} and Co^{2+} ions were segregated into the grain boundary region.

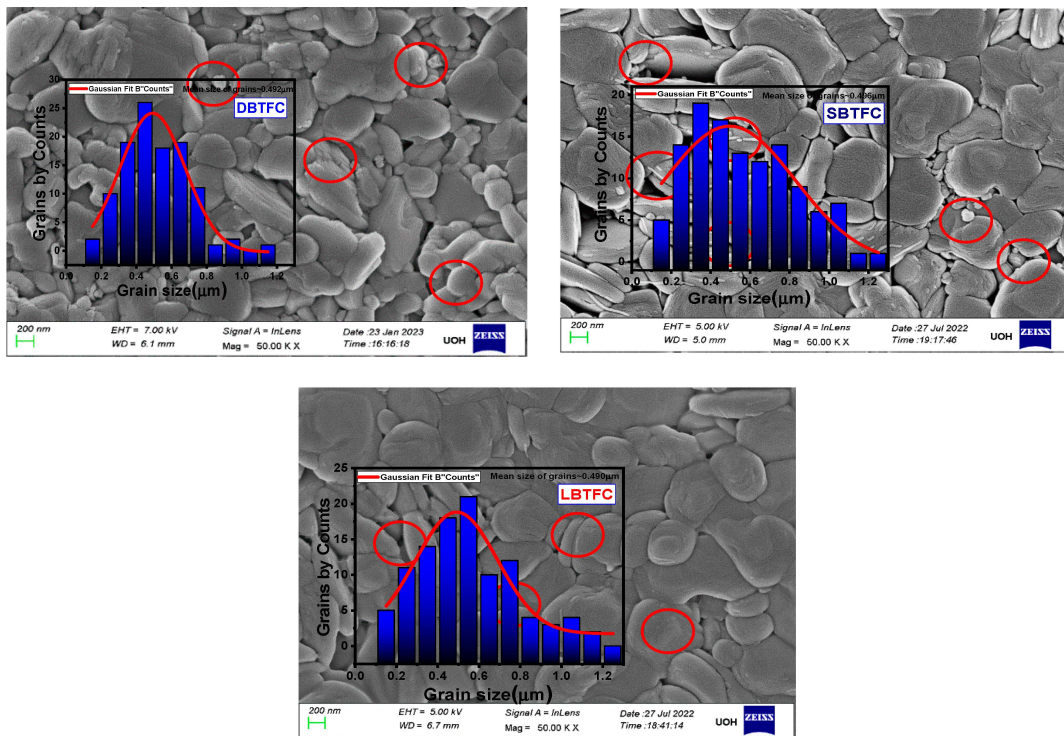


Figure 2. FESEM photographs of DBTFC, SBTFC, and LBTFC; Insets in figures: Histograms of the samples. Inset: Histograms corresponding to grain sizes.

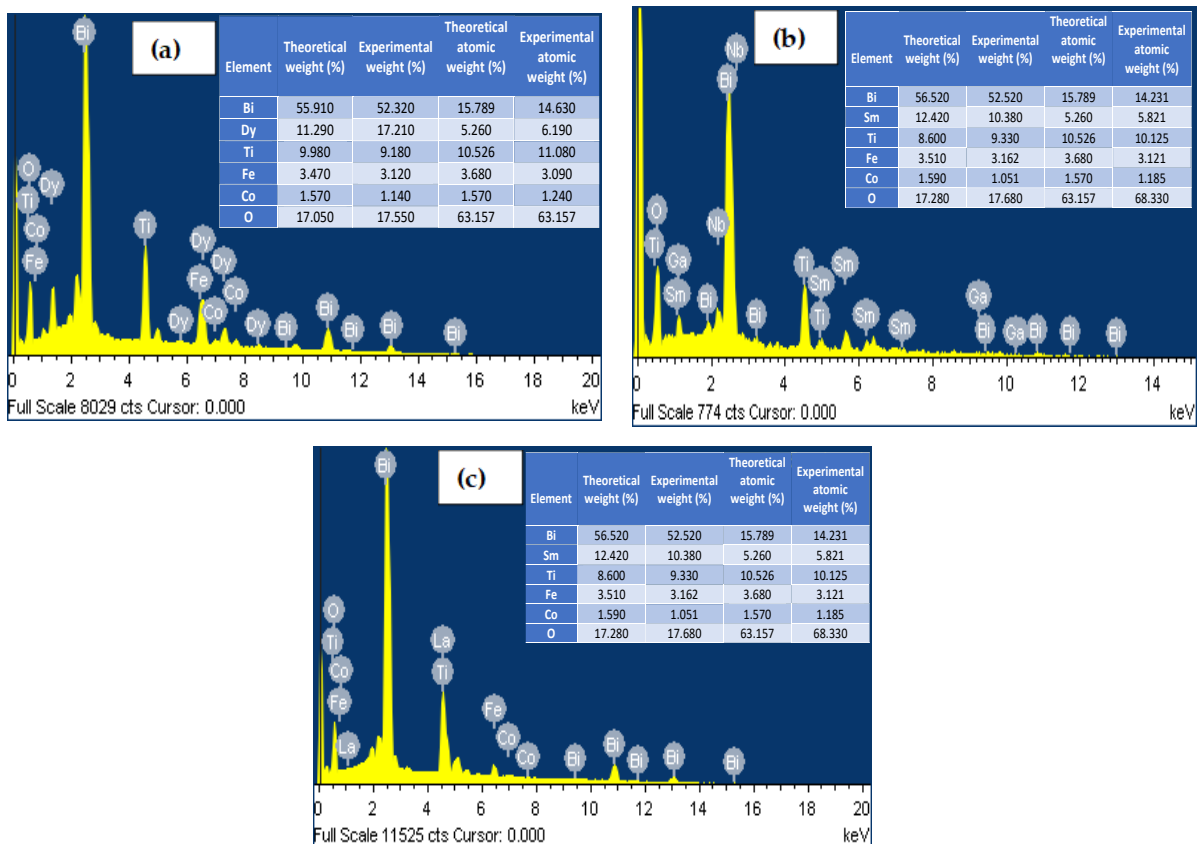


Figure 3. EDAX patterns of (a) DBTFC, (b) SBTFC, and (c) LBTFC; Insets in figures: Elemental analysis of samples.

3.3. Raman Spectroscopic Studies

Raman scattering spectra of the prepared ceramics are shown in Figure 4a–c to investigate lattice vibrational modes, lattice distortion, and occupancy of doped ions at the specified A- and B-sites. All observed modes of the prepared samples showed similar characteristic modes of the orthorhombic structure of three-layered Aurivillius compounds [57,62,63]. The overlapped peaks were de-convoluted using Lorentzian peak fittings, for better identification of peak positions. The Raman modes ν_1 , ν_2 , and ν_3 below 200 cm^{-1} were attributed to the A-site of ABO_3 perovskite blocks' cation vibrations. Slight changes observed for SBTFC, below 200 cm^{-1} , were associated with the vibration of Bi^{3+} ions of $(\text{Bi}_2\text{O}_2)^{2-}$ layer slabs. Changes observed below 200 cm^{-1} for SBTFC were due to strains caused in the layer-perovskite slabs. The phonon modes at high frequencies in the range of $200\text{--}800\text{ cm}^{-1}$ were attributed to the vibrational modes of BO_6 octahedral [64]. The Raman modes ν_4 , ν_5 , and ν_6 (around 225 cm^{-1} , 260 cm^{-1} , and 312 cm^{-1}) demonstrated the torsional bending of BO_6 octahedral. The phonon modes ν_7 , ν_8 , and ν_{13} were ascribed to the stretching of the O–Ti/O–Fe/O–Co bond. The broad peaks, namely ν_7 , ν_8 , and ν_{13} , were used to reveal the site occupancies of doped ions in the proposed sites. The broadening of the peaks by merging ν_8 , and ν_9 for the SBTFC sample was due to the inhomogeneous distribution in the compositions of the A- and B-sites of perovskite blocks. Finally, this in turn led to lattice distortion. From this, one can say that the RE and Co/Fe ions readily occupy the A- and B-sites of perovskites [50,65]. The Raman modes ν_4 , ν_5 , and ν_6 were found to vary slightly depending on the RE ion. The same phenomenon was observed in vibration modes above 200 cm^{-1} for SBTFC. This was once again attributed to the lattice distortion caused by Fe and Co ion doping in Ti-sites of BO_6 octahedral. The phonon modes ν_{10} and ν_{11} , around 730 cm^{-1} in all samples, were attributed to the FeO_6 and CoO_6 octahedral. Based on this, one can say that the Fe and Co ions are partially occupied by the Ti-sites of the perovskite blocks.

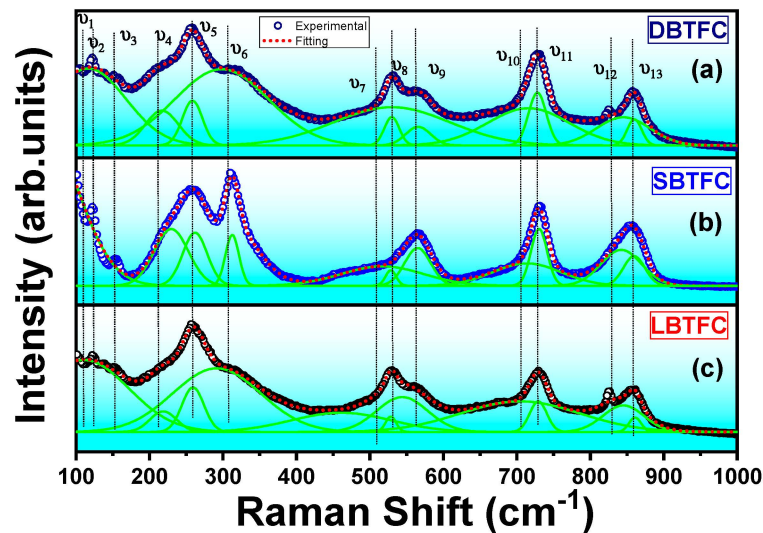


Figure 4. Raman spectra of (a) DBTFC, (b) SBTFC, and (c) LBTFE with peak fitting.

3.4. Dielectric Studies

The dielectric measurements of all compounds were carried out on the three samples at different frequencies and shown in Figure 5a–c. The variation of dielectric loss ($\tan \delta$) with the temperature in the range of 30 to $500\text{ }^\circ\text{C}$ at 10 kHz , 20 kHz , 30 kHz , 50 kHz , and 100 kHz frequencies are shown in the inset of Figure 5a–c. The higher the temperature was, the greater the dielectric constant. A notable dielectric dispersion observed with frequency at high temperatures was due to the presence of thermally activated polarization of charge species such as space charges, charge defects, and oxygen vacancies. A slow increase of dielectric nature especially in the DBTFC sample indicated the presence of

oxygen vacancies, as pointed out by many researchers. Temperature independent of the dielectric constant up to 250 °C was attributed to the hopping conduction mechanism in between the neighboring sites of Ti^{3+} and Ti^{4+} or Fe^{2+} and Fe^{3+} . Typically, the formation of dipoles with doubly ionized oxygen vacancies (V''_O) is less likely than singly ionized oxygen vacancy (V'_O). The doubly ionized oxygen vacancies (V''_O) and electrons together create defective or complex dipoles, such as $Fe^{3+} - V''_O$, $Co^{3+} - V''_O$, and $Ti^{4+} - V''_O$. The doubly ionized oxygen vacancies predominate in the conduction process over mono ionized oxygen vacancies [66–68]. Generally, the dielectric transition temperature of ceramics depends on complex or defective ions. Since the measurements were carried out in the range of 30 to 500 °C, the transition temperatures (T_C) of all samples could not be observed. It was observed that Fe-/Co-doped $Bi_4Ti_3O_{12}$ compounds showed transition temperatures [67–70]. In the present analysis, SBTFC compounds showed a higher dielectric constant than DBTFC and LBTFC. This may be due to an increase in the interfacial or space charge polarization. This increase in the interfacial polarization was observed in the FESEM images (Figure 3). This reveals a decrease in grain size in SBTFC. The decrement in grain size led to an increase in the interfacial charges due to an increment in the volume fraction of grain boundaries. The same phenomenon was also applicable to the DBTFC and LBTFC samples. A similar conclusion can be inferred from the variation of dielectric loss as a function of temperature, as shown in the inset of Figure 5a–c.

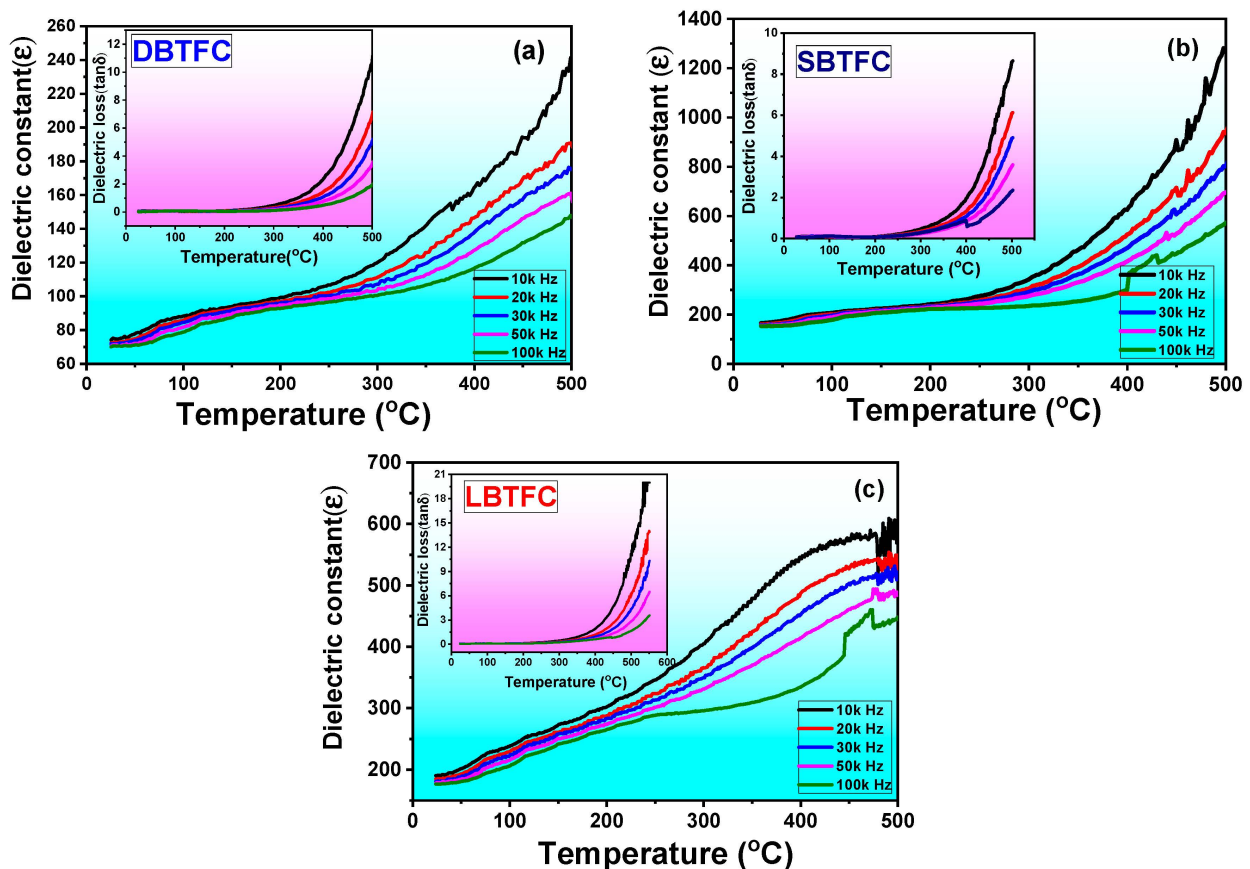


Figure 5. Variation of dielectric constant with temperature of (a) DBTFC, (b) SBTFC, and (c) LBTFC; Insets in figures: dielectric loss vs. temperature.

3.5. Electrical Studies

AC-conductivity analysis was performed for a better understanding of the transport mechanism in the samples. Figure 6a–c depicts the AC-conductivity (σ_{ac}) as a function of

frequency plots (f) at various temperatures. The AC-conductivity data were obtained by considering the following expression [69].

$$\sigma_{ac} = \left[\frac{Z'}{Z'^2 + Z''^2} \right] \left(\frac{d}{S} \right) \quad (2)$$

where σ_{ac} is AC-conductivity, and Z' and Z'' are real and imaginary values of impedance. The terms d and S denote the thickness and area of the sample respectively. The AC-conductivity data were found to obey the following Jonscher's power law [69]

$$\sigma_{ac} = \sigma_{dc} + A(T)\omega^n \quad (3)$$

where σ_{ac} is ac conductivity, σ_{dc} is DC-conductivity, $A(T)$ is temperature dependent coefficient, and the exponent n represents slope. The term $A(T)\omega^n$ characterizes the dispersion phenomena observed in the sample, and ω is the angular frequency. The exponent n is a dimensionless quantity that generally lies between 0 and 1. This quantity depicts the degree of interaction between mobile ions and the surrounding lattice. Attempts were made to fit the AC-conductivity data with Equation (2), but no data were found to fit successfully throughout the frequency region. From the AC-conductivity plots, we can observe two regions, namely high-frequency and intermediate-frequency regions, as shown in Figure 6a–c. The AC-conductivity in the low frequency (region-I) is merely independent of frequency. To account for better fitting, the experimental data have been fitted with the following relation [69]:

$$\sigma_{ac} = \sigma_{dc} + A(T)\omega^{n_1} + B(T)\omega^{n_2} \quad (4)$$

where n_1 ($0 < n_1 < 1$) and n_2 ($1 < n_2 < 2$) are frequency exponents, which give slopes of corresponding regions. The exponent n_1 depicts the intermediate-frequency dispersion attributing to the ion hopping mechanism. The exponent n_2 describes high-frequency dispersion, attributing to the localized relaxation process [70–72]. The experimental data were in good agreement with fitting data using Equation (4) as shown in Figure 6a–c. The AC-conductivity of all samples was strongly independent of frequencies above 400 °C. The AC-conductivity $\leq 10^4$ Hz was independent of frequency (ω) at all temperatures and provided DC-conductivity. At a temperature below 400 °C, the AC-conductivity became strongly dependent on frequency for all samples. Strong coalitions or merging into a single curve at higher frequencies for all samples indicated the migration of oxygen vacancies. The exponent values n_1 and n_2 were plotted against temperature (Figure 6d).

The frequency-independent conductivity at lower frequencies for all samples can be illustrated using the ion-jump relaxation model [73,74]. The defective ions, which were oxygen vacancies, hopped between their neighborhood vacant sites of Ti^{3+} and Ti^{4+} . This hoping of ions may take a long time and results in a long-range transitional motion of ions. This process is called the DC-conductivity of the samples. The correlated barrier hopping model can generally explain the frequency-dependent conductivity. It was deduced from the fitting, shown in Figure 6d, that the frequency exponent n_1 decreased with increasing temperature. A cation in the lattice was hopping either a forward or backward vacant site. Thermally active oxygen vacancies yield to more dispersive nature at lower frequencies [75]. Frequency exponent n illustrates the motion or localization of charge carriers in the samples. In region-I (R1), where $0 < n_1 < 1$, the charge carriers can have translation motion and a sudden long-hop takes place, whereas $1 < n_2 < 2$ illustrates a localized relaxation or hopping mechanism in the vicinity of lattice sites. Here, exponent n_1 values are less than 1, so the charge carriers have translational ion hopping within the ceramics [71,76,77]. On the other side, the values of n_2 are greater than 1 at a higher frequency range, which illustrates the existence of a localized relaxation process. From this analysis, one can speculate that the conductivity is mainly due to short-range hopping or a kind of competitive interaction via doubly ionized oxygen vacancies.

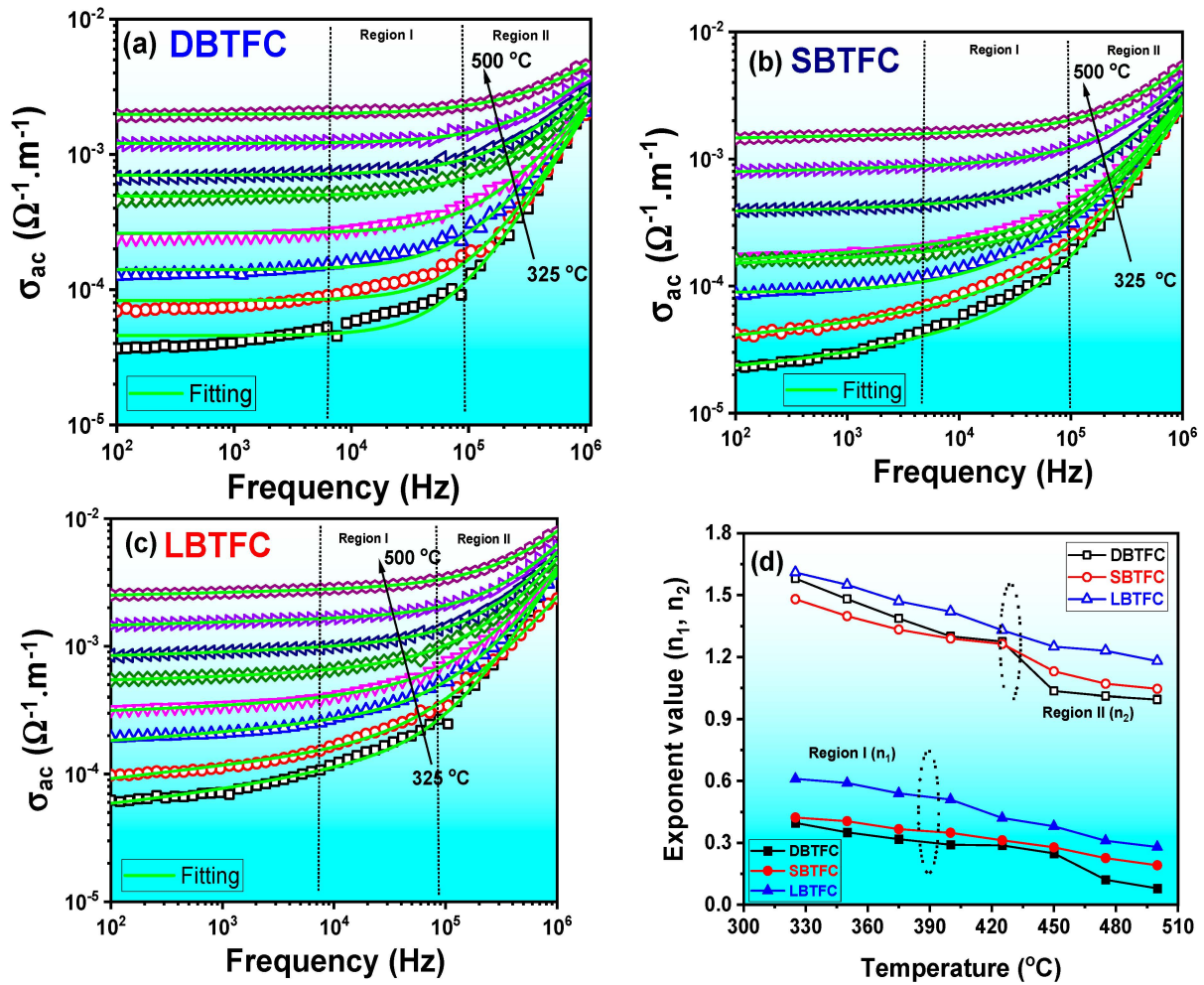
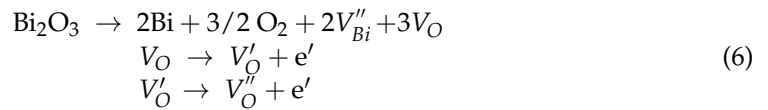


Figure 6. Variation of AC-conductivity with the frequency of (a) DBTFC, (b) SBTFC, and (c) LBTFC; (d) exponent values (n_1, n_2) vs. temperature. Slopes measured in region-I (lower) and region-II (upper) are marked as dotted circles.

The DC-conductivity of the samples was calculated from AC-conductivity plots by extrapolating the frequency-independent term to 1 Hz. Figure 7 shows DC-conductivity as a function of temperature. The increase in conductivity with increasing temperature indicates the negative temperature coefficient of resistance behavior. The variation of DC-conductivity with temperature can explain the overall conduction (bulk) of the samples. The activation energies were calculated using the following Arrhenius relation:

$$\sigma_{dc} = \sigma_0 e^{-E_a/KT} \quad (5)$$

where σ_{dc} is DC-conductivity, E_a is activation energy, T is temperature, and K is Boltzmann constant. The variation of DC-conductivity plots reveals the conduction of a thermally activated rotation of dipoles. From the plots, activation energies were observed to be 0.931, 0.828, and 0.807 eV for DBTFC, SBTFC, and LBTFC, respectively. From the previous reports, the activation energies of Aurivillius compounds were observed to lie in the order of 0.87–1.4 eV. The present activation energy values were in good agreement with previous reports [78]. Aurivillius phase compounds have the volatile nature of bismuth during high sintering temperatures. To conserve charge neutrality, certain oxygen loss occurs, as per the following Kroger–Vink notations:



where, V''_{Bi} is doubly ionized bismuth vacancy, e' is electron released, and V'_{O} and V''_{O} are singly and doubly ionized oxygen vacancies, respectively. The overall conductivity can be attributed to oxygen vacancies and ion charge fluctuations. The ion charge fluctuations in the present samples can be explained as follows:

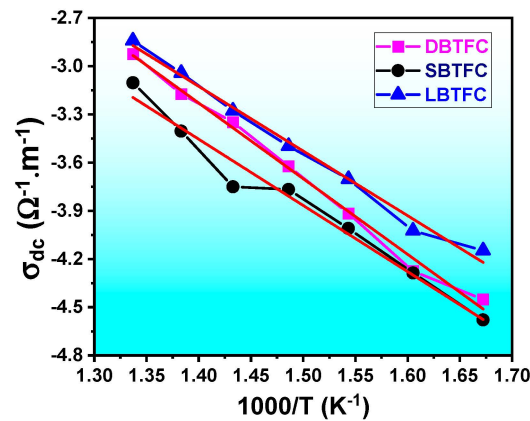


Figure 7. Variation of DC-conductivity with 1000/Temperature (°C) of DBTFC, SBTFC, and LBTFC.

From the above equations, Fe^{2+} and Ti^{4+} sites form dipoles with vacant defects (oxygen vacancy). These dipoles try to orient themselves using an electron-hopping mechanism. The charge carriers get trapped near localized sites and may form large polarons. The same phenomenon can apply to the Fe^{2+} ions, where the conduction mechanism is attributed to small polarons.

Another aspect of the above defect mechanism can be illustrated by complex impedance curves (Cole–Cole) as shown in Figure 8a–c. The first big and second small semi-circles represent the grain (g) and grain boundary (gb) contribution of the samples. Large grain resistance (R_g) indicates defects such as oxygen vacancies and complex dipoles at grain interfaces. This interim affects the single domain or ferroelectric nature of the samples. All fitting parameters are depicted in Table 3. The inset of Figure 8a–c exhibits the room temperature hysteresis (polarization vs. electric field) loops of the DBTFC, SBTFC, and LBTFC samples under the applied strengths of 500 V/cm, 750 V/cm, and 1000 V/cm with a constant frequency of 50 Hz. The unsaturated loops revealed very high coercive and saturation fields. Generally, the Aurivillius phase compounds showed low remanent polarization and high coercive and saturation fields. In addition, the polarization of Aurivillius phase compounds depended on factors such as crystal symmetry, strain effects, phase transitions, and the competition of dopants. The Aurivillius phase compounds caused lattice distortion in the BO_6 octahedron, which affected the electric dipole moments [57]. The asymmetric and unsaturated ferroelectric hysteresis (P-E) loops illustrated the leaky nature or accounted for the presence of a greater number of oxygen vacancies or defective charge carriers. It is a known fact that ferroelectric (hysteresis) nature is considered as a collective nature rather than a single ionic migration. Since the overall conductivity was due to the migration of oxygen vacancies or complex defect dipoles at lower temperatures, a saturated hysteresis loop could not be obtained. This result was an enhancement of the magnetic nature of the samples. From this $\text{Bi}_{3.25}\text{La}_{0.75}\text{Ti}_3\text{O}_{12}$ impedance data observation, it is evident that complex-defect dipoles, which were accumulated at the grain interfaces,

became relaxed easily during the conduction mechanism. Therefore, similar compound $\text{Sm}_{0.75}\text{Bi}_{3.25}\text{Ti}_{2.9625}\text{V}_{0.03}\text{O}_{12}$ (SBVT), rare-earth doped Aurivillius multiferroics showed well-saturated P-E loops [59,79]. This suggests that when Ti^{4+} ions were replaced by Fe^{3+} or Co^{3+} , these defective charge complexes were trapped by the oxygen vacancies, so higher electric fields were required to activate these trapped charges to acquire saturated P-E hysteresis loops. Within the applied electric fields, all samples showed less loss nature.

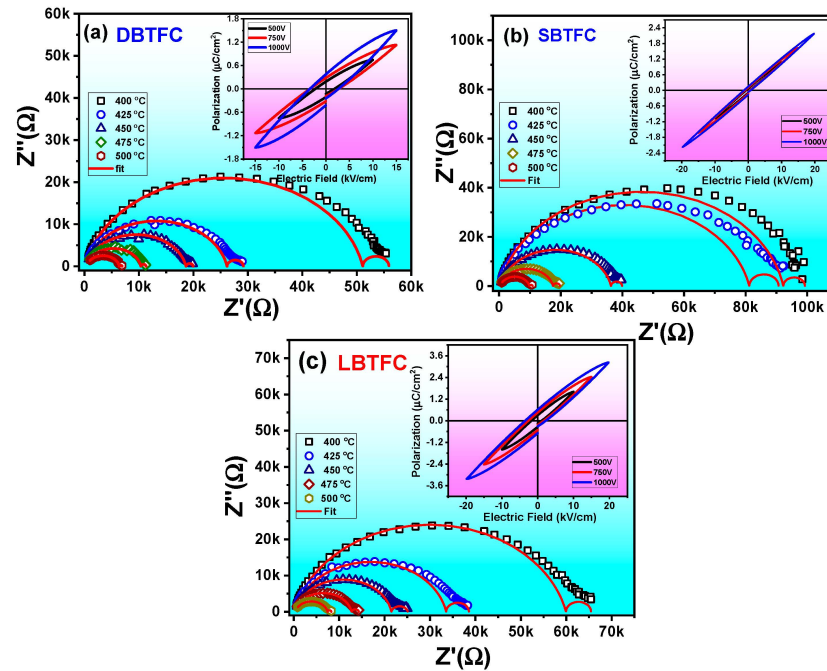


Figure 8. Complex impedance (Cole–Cole) plots of (a) DBTFC, (b) SBTFC, and (c) LBTFC; Insets in figures: P vs. E loops.

Table 3. Complex impedance fitting parameters of the DBTFC, SBTFC, and LBTFC sample.

DBTFC								
No.	Temperature (°C)	R_1 (Ω)	R_2 (Ω)	CPE-1	n	R_3 (Ω)	CPE-2	n
1	400	200	92,000	5.200×10^{-10}	0.885	7000	3.40×10^{-4}	1
2	425	240	84,000	7.500×10^{-10}	0.87	6500	4.20×10^{-4}	1
3	450	320	36,000	6.200×10^{-10}	0.875	3600	4.60×10^{-4}	1
4	475	340	17,200	4.9×10^{-10}	0.88	2200	4.65×10^{-4}	1
5	500	360	9500	7.80×10^{-10}	0.86	1050	5.20×10^{-4}	1
SBTFC								
No.	Temperature (°C)	R_1 (Ω)	R_2 (Ω)	CPE-1	n	R_3 (Ω)	CPE-2	n
1	400	100	51,000	6.100×10^{-10}	0.877	4800	9.9×10^{-4}	1
2	425	180	26,000	5.700×10^{-10}	0.882	3000	9.1×10^{-4}	1
3	450	250	18,400	5.500×10^{-10}	0.885	1300	8.2×10^{-4}	1
4	475	350	10,100	4.400×10^{-10}	0.895	950	7.9×10^{-4}	1
5	500	380	6041	5.300×10^{-10}	0.90	480	7.8×10^{-4}	1
LBTFC								
No.	Temperature (°C)	R_1 (Ω)	R_2 (Ω)	CPE-1	n	R_3 (Ω)	CPE-2	n
1	400	150	59,800	9.900×10^{-10}	0.862	6000	5.0×10^{-4}	1
2	425	280	33,284	6.400×10^{-10}	0.880	5000	4.1×10^{-4}	1
3	450	300	21,200	6.200×10^{-10}	0.89	3600	4.5×10^{-4}	1
4	475	320	12,400	6.1×10^{-10}	0.886	1600	4.7×10^{-4}	1
5	500	350	7100	9.50×10^{-10}	0.86	800	5.2×10^{-4}	1

3.6. Magnetic Studies

Figure 9a–c shows the variation of magnetization with the applied magnetic field (M-H loops) for all DBTFC, SBTFC, and LBTFC samples obtained at room temperature. Small hysteresis loop areas indicate a canted antiferromagnetic (AFM) nature. This nature correlates to the tilt-canted magnetic dipole moments. It should be noted that the canted nature of two sub-lattices yields a small hysteresis loop area. These materials consist of spontaneous magnetized domains. These materials possess low retentivity and coercivity values even at high magnetic fields. The introduction of magnetic ions Ni/Fe/Co in the B-site of Aurivillius phases raised the spontaneous magnetization [80]. The magnetization in the Co-/Fe-doped Aurivillius phase compounds main contributions, viz (i) exchange interactions between the neighboring ions like $\text{Fe}^{3+}-\text{O}-\text{Co}^{2+}$ or $\text{Fe}^{3+}-\text{O}-\text{Co}^{3+}$ in iron-rich regions, and (ii) tilt-canted spins or antisymmetric DM (Dzyaloshinskii–Moriya) interactions. Three-layered single-phase Aurivillius compounds with orthorhombic Fmmm structure exhibited AFM or weak ferromagnetism, which emerged from the localized magnetic (Fe/Co) rich regions. This suggests a super-exchange interaction between neighboring Fe and Co ions via oxygen vacancies [81,82]. This can also be due to the long-range magnetic order in the ceramics. The structure evolution and Fe/Co—O—Co/Fe bond angles in ABO_3 perovskites in the layered compounds also affect the magnetization of the ceramics. To understand more about FM nature, the following law of approach is used [79,80]:

$$M = M_S \left[1 - \frac{A}{H} - \frac{B}{H^2} \right] + \chi_P H_K \quad (8)$$

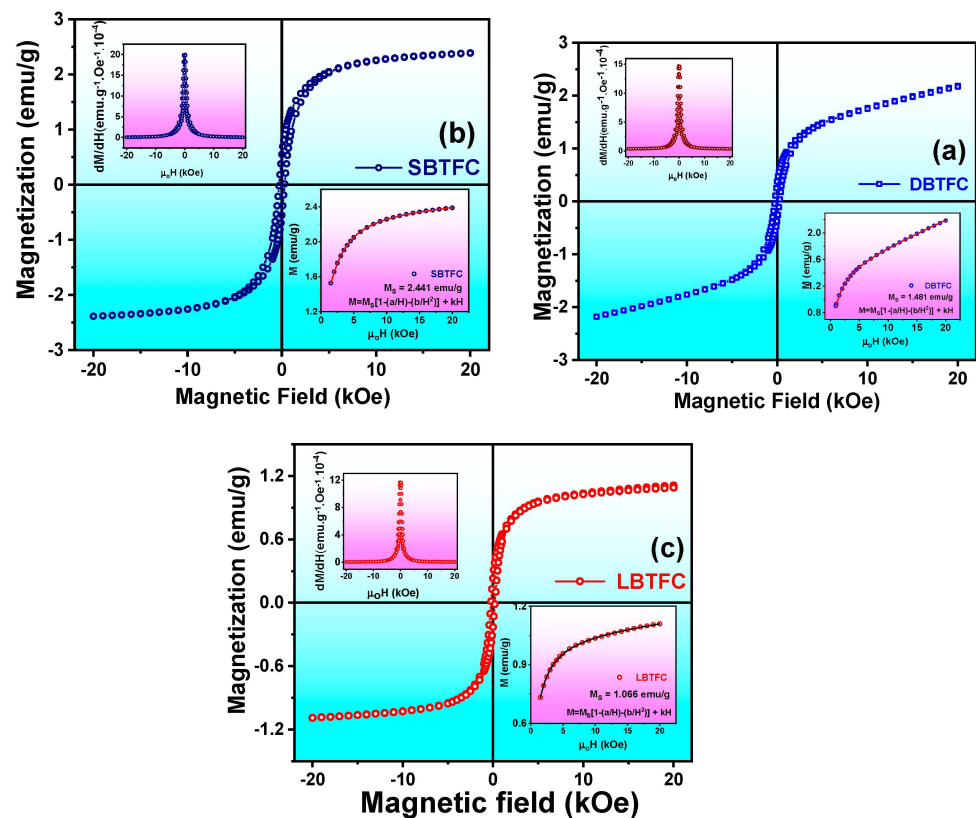


Figure 9. Room-temperature magnetic hysteresis loops of (a) DBTFC, (b) SBTFC, and (c) LBTFC; Insets in figures (left): derivation of magnetization (dM/dH) vs. applied magnetic field; Insets in figures (right): law of approach to saturation fittings M vs. H curves of DBTFC, SBTFC, and LBTFC samples.

The term $\frac{A}{H}$ represents the inhomogeneity of magnetization; $\chi_P H_K$ is the forced field-induced magnetization; and $\frac{B}{H^2}$ parameters explain magneto-anisotropic nature. By

considering the importance of the above LAS, Equation (8) is fitted in the low magnetic field regions and shown in the inset of Figure 9a–c. By using Equation (8), the output of fitting curves (R^2) was found to be ~ 0.99 and thus the results of fitting were highly reliable.

In the present investigation, the DBTFC sample showed an unsaturated hysteresis nature, indicating a combination of both FM and AFM [83]. The formation of Bi–O–Dy bonds enhances magnetization. The Sm^{3+} -doped REBTFC sample showed a higher value of magnetization. The results are consistent with our recent work on rare-earth modified Aurivillius intergrowths whose magnetization follows the similar rare-earth dependence [57]. The magnetic moment per formula unit ($\mu_{f.u.}$) in the Bohr Magnetron is calculated using the following formula:

$$\mu_{f.u.}(\text{in } \mu_B) = \frac{M * \text{mol.weight} * \text{conversion factor}}{N * \mu_B} \quad (9)$$

where M (emu/g) is measured magnetization from the fitting of the law of saturation (shown in the 4th quadrant of Figure 9); mol. weight (g) is the molecular weight of the formula; μ_B is the Bohr magnetron; 9.274×10^{-24} J/T, N is Avogadro's number = 6.023×10^{23} ; and the conversion factor is 10^{-3} J/T. The magnetic moment per formula units (in μ_B) for DBTFC, SBTFC, and LBTFC were found to be 0.30, 0.49, and 0.21 μ_B , respectively. The SBTFC sample exhibited remanent magnetization ($2M_r$) of about 550×10^{-3} emu/g at room temperature, which was bigger than the earlier reported value [84,85]. The inset of Figure 9a–c (left) illustrates the plots of the derivation of magnetization (dM/dH) as a function of the applied magnetic field. It can be noticed that a single sharp peak is observed in all curves. This can be attributed to the behavior of soft kind magnetism and uniform magnetic grain nature. A single sharp peak is observed in the left side inset of Figure 9a–c. From this, one can anticipate that all prepared samples were of a soft magnet.

3.7. Magnetoelectric Studies

The variation of the magnetoelectric (ME) coefficient with the applied magnetic field of prepared samples is shown in Figure 10. The values of the magnetoelectric coefficient were found to be 42.4 mV/cm-Oe, 30.3 mV/cm-Oe, and 21.6 mV/cm-Oe for DBTFC, LBTFC, and SBTFC, respectively.

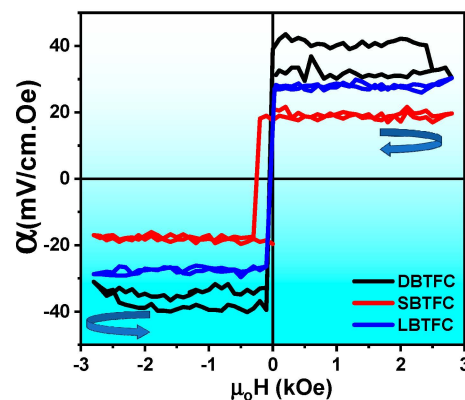


Figure 10. ME coefficient vs. applied magnetic field plots of DBTFC, SBTFC, and LBTFC samples.

It is observed from the previous reports that the $\text{Bi}_4\text{Ti}_3\text{Fe}_{0.7}\text{Co}_{0.3}\text{O}_{15}$ (BFTO) sample showed an ME coefficient of $16.45 \text{ mV cm}^{-1}\text{Oe}^{-1}$ [64,86]. The obtained ME values of the prepared samples were found to be higher compared to the other Aurivillius compounds. Furthermore, the high ME coefficient was obtained at lower magnetic fields (3 kOe), as shown in Figure 10. The ME coupling mainly arises from two aspects, namely, (i) spin-exchange or spin-orbit interactions, driven by inverse DM interaction, and (ii) spin-lattice interaction. The contribution of spin-orbit or spin-exchange interaction via inverse DM interactions is smaller than the spin-lattice interactions [87]. In particular, the magnetic ions

in BO_6 octahedral sites are slightly shifted from their regular sites under the application of a magnetic field. This induces a strain in the lattice structure and develops the voltage via ferroelectric accumulated changes. However, further studies are needed to establish the plausible reason for obtaining a high ME coefficient. As it is reported, the impurity phases of Co/Fe compositions influence the ME nature in Aurivillius compounds [57]. The presence of circled regions of SEM micrograph dots (nanoregions) represents a Co/Fe-rich magnetic phase. Based on these observations, such Co/Fe-rich phases could contribute partly to the enhanced ME properties of the prepared samples.

In particular, when an external magnetic field is applied, the magnetic ions are slightly displaced from their normal octahedral position, which induces a voltage in the lattice, resulting in ferroelectric and ferroelastic changes, and finally producing an output voltage. The parameters of orthorhombic distortion, tetragonal stain, and orthorhombicity play a significant role in ME properties [88]. In our study, the DBTFC sample showed higher ME coefficients. This is in good agreement with the lattice structure of the prepared samples. Higher orthorhombicity and lower orthorhombic distortion values were observed for the Dy-doped sample (DBTFC), which are favorable to enhancing the ME coefficient under magnetic fields. In this study, the RE (Dy, La, and Sm) element substitution in the A-site of Aurivillius compounds induced lattice distortion, and it led to accompanying electric polarization under magnetic fields. It can be concluded that the RE-doped three-layered Aurivillius phase compounds show strong ME coupling. These multiferroic materials are useful for understanding the ME phenomenon.

4. Conclusions

In summary, we investigated the structural, morphological, electrical, magnetic, and magnetoelectric properties of the RE-doped (Dy, Sm, and La) $\text{Bi}_3\text{RETi}_2\text{Fe}_{0.7}\text{Co}_{0.3}\text{O}_{12-\delta}$ Aurivillius multiferroic compounds. The XRD and Raman spectroscopic studies revealed that the prepared samples were formed in single phase and orthorhombic structure with space group $Fmmm$. This revealed that the ions were properly substituted into lattice cells. The plate-like, anisotropic, randomly orientated grains were observed in FESEM studies, which is a characteristic feature of Aurivillius phase ceramics. The substitution of RE significantly enhanced the dielectric and ferroelectric properties with improved dielectric constants in the frequency range, and reduced dielectric loss values were found at lower frequency ranges. Improved remanent polarization was observed in all samples at room temperature. This is attributed to the reduction in the oxygen vacancies by doping RE in the Bi-sites of the samples. Ferroelectric and magnetic studies revealed good multiferroic behavior in the samples. The M-H loops of the samples suggested an exchange interaction between adjacent ions or DM interactions among magnetic ions. Strong ferroelectric-magnetic coupling accompanied by a high coefficient of magnetoelectric coupling of 42.4 mV/cm-Oe was exhibited by the DBTFC sample. This strong ME coefficient in a single phase may be applicable in multiferroic devices and can be interpreted from the perspective of previous studies and of the working hypotheses.

Author Contributions: Conceptualization: V.V., N.V.P. and E.V.R.; Methodology: V.V. Data curation, V.V., V.S.P., S.S. and S.N.B.; Writing—original draft preparation V.V.; writing and reviewed work: N.V.P., E.V.R., G.S. and G.P.; Supervision: N.V.P., E.V.R. and G.P. All authors have read and agreed to the published version of the manuscript.

Funding: This work was partially supported by OU-DST PURSUE-II/80/2021, project ARDB/01/2032004 and CSIR-HRDG, No: 09/132(0875)/2018-EMR-I, New Delhi for providing fellowship. National Science Foundation (NSF) (ECCS-1923732, ECCS-EAGER-2236879, DMR-1808892) and the Air Force Office of Scientific Research (AFOSR) Award No. FA9550-20-1-0114.

Data Availability Statement: Data is contained within the article.

Acknowledgments: One of the authors (V.V) is thankful to CSIR-HRDG, New Delhi for providing JRF/SRF (File No: 09/132(0875)/2018-EMR-I). One of the authors (N.V.P) acknowledges the funding by ARDB/01/2032004, OU-DST PURSUE-II/80/2021, SIR-HRDG and 09/132(0875)/2018-EMR-I, New Delhi. EVR (032-88-ARH/2018) acknowledges the Portuguese Foundation for science and Technology (FCT) for financial assistance through national funds (OE), in the scope of the framework contract foreseen in the numbers 4, 5, and 6 of article 23 of the Decree-Law 57/2016, of August 29, changed by Law 57/2017, of July 19. The research at Oakland University was supported by grants from the National Science Foundation (NSF) (ECCS-1923732, ECCS-EAGER-2236879, DMR-1808892) and the Air Force Office of Scientific Research (AFOSR) Award No. FA9550-20-1-0114.

Conflicts of Interest: The authors declare no conflicts of interest.

References

1. Nan, C.W.; Bichurin, M.I.; Dong, S.; Viehland, D.; Srinivasan, G. Multiferroic magnetoelectric composites: Historical perspective, status, and future directions. *J. Appl. Phys.* **2008**, *103*, 031101. [[CrossRef](#)]
2. Bibes, M.; Barthélémy, A. Multiferroics: Towards a magnetoelectric memory. *Nat. Mater.* **2008**, *7*, 425. [[CrossRef](#)]
3. Dong, S.; Liu, J.M.; Cheong, S.W.; Ren, Z. Multiferroic materials and magnetoelectric physics: Symmetry, entanglement, excitation, and topology. *Adv. Phys.* **2015**, *64*, 519. [[CrossRef](#)]
4. Fiebig, M.; Lottermoser, T.; Meier, D.; Trassin, M. The evolution of multiferroics. *Nat. Rev. Mater.* **2016**, *1*, 16046. [[CrossRef](#)]
5. Khomskii, D. Classifying multiferroics: Mechanisms and Effects. *Physics* **2009**, *2*, 20. [[CrossRef](#)]
6. Spaldin, N.A. Multiferroics: Past, present, future. *MRS Bull.* **2017**, *42*, 385. [[CrossRef](#)]
7. Jana, B.; Ghosh, K.; Rudrapal, K.; Gaur, P.; Shihabudeen, P.K.; Roy Chaudhuri, A. Recent Progress in Flexible Multiferroics. *Front. Phys.* **2022**, *9*, 822005. [[CrossRef](#)]
8. Scott, J.F. Data storage: Multiferroic memories. *Nat. Mater.* **2007**, *6*, 256. [[CrossRef](#)]
9. Kreisel, J.; Kenzelmann, M. Multiferroics—The challenge of coupling magnetism and ferroelectricity. *Europhys. News* **2009**, *40*, 17. [[CrossRef](#)]
10. Sahoo, R.R.; Choudhary, R.N.P. Effect of Ce infusion on the structural, dielectric, optical, transport and polarization behavior of Nd-modified triple-layered Aurivillius phase ceramic $\text{Bi}_3\text{NdTi}_3\text{O}_{12}$. *Ceram. Int.* **2024**, *50*, 205. [[CrossRef](#)]
11. Subbarao, E.C. A family of ferroelectric bismuth compounds. *J. Phys. Chem. Solids* **1962**, *23*, 665. [[CrossRef](#)]
12. Wang, G.; Huang, Y.; Sun, S.; Wang, J.; Peng, R.; Lu, Y.; Tan, X. Layer Effects on the Magnetic Behaviors of Aurivillius Compounds $\text{Bi}_{n+1}\text{Fe}_{n-3}\text{Ti}_3\text{O}_{3n+1}$ ($n = 6, 7, 8, 9$). *J. Am. Ceram. Soc.* **2016**, *99*, 1318. [[CrossRef](#)]
13. Khomchenko, V.A.; Kakazei, G.N.; Pogorelov, Y.G.; Araujo, J.P.; Bushinsky, M.V.; Kiselev, D.A.; Kholkin, A.L.; Paixão, J.A. Effect of Gd substitution on ferroelectric and magnetic properties of $\text{Bi}_4\text{Ti}_3\text{O}_{12}$. *Mater. Lett.* **2010**, *64*, 1066. [[CrossRef](#)]
14. Hou, D.; Fan, H.; Chen, Y.; Jia, Y.; Wang, W. Effects of lanthanide ions on the structure and electrical properties of Aurivillius $\text{Bi}_3\text{TiNbO}_9$ high temperature piezoelectric ceramics. *J. Alloys Compd.* **2022**, *921*, 166065. [[CrossRef](#)]
15. Sun, J.; Han, Y.; Gao, G.; Yang, J.; Zhang, Y.; Dai, Y.; Song, D. Breakdown field enhancement and energy storage performance in four-layered Aurivillius films. *Ceram. Int.* **2022**, *48*, 15780. [[CrossRef](#)]
16. Li, Z.; Koval, V.; Mahajan, A.; Gao, Z.; Vecchini, C.; Stewart, M.; Cain, M.G.; Tao, K.; Jia, C.; Viola, G.; et al. Room-temperature multiferroic behavior in layer-structured Aurivillius phase ceramics. *Appl. Phys. Lett.* **2020**, *117*, 52903. [[CrossRef](#)]
17. Supriya, S. Effect of doping and enhanced microstructures of bismuth titanates as Aurivillius perovskites. *Micron* **2022**, *162*, 103344. [[CrossRef](#)]
18. Kikuchi, T.; Watanabe, A.; Uchida, K. *A Family of Mixed-Layer Type Bismuth Compounds*; Pergamon Press, Inc.: Oxford, UK, 1977; Volume 12, p. 299.
19. Zhao, H.; Cai, K.; Cheng, Z.; Jia, T.; Kimura, H.; Ma, Z.; Fu, Q.; Huang, Z.; Matsumoto, T.; Tohei, T.; et al. A novel class of multiferroic material, $\text{Bi}_4\text{Ti}_3\text{O}_{12} \cdot n\text{BiFeO}_3$ with localized magnetic ordering evaluated from their single crystals. *Adv. Electron. Mater.* **2017**, *3*, 1600254. [[CrossRef](#)]
20. Veenachary, V.; Puli, V.S.; Babu, S.N.; Prasad, G.; Prasad, N.V. Electrical and magnetic studies on promising Aurivillius intergrowth compound. *J. Mater. Sci. Mater. Electron.* **2022**, *33*, 22614. [[CrossRef](#)]
21. Koval, V.; Shi, Y.; Skorvanek, I.; Viola, G.; Bures, R.; Saksl, K.; Roupčova, P.; Zhang, M.; Jia, C.; Yan, H. Cobalt-induced structural modulation in multiferroic Aurivillius-phase oxides. *J. Mater. Chem. C* **2020**, *8*, 8466. [[CrossRef](#)]
22. Yin, Y.; Liu, F.; Mao, X.; Wang, W. Multiferroic properties of $\text{Bi}_{5.75}\text{R}_{0.25}\text{Fe}_{1.4}\text{Ni}_{0.6}\text{Ti}_3\text{O}_{18}$ ($\text{R} = \text{Eu}, \text{Sm}, \text{Nd}, \text{Bi}$ and La) ceramics. *J. Rare Earths* **2022**, *40*, 112. [[CrossRef](#)]
23. Hou, R.Z.; Chen, X.M.; Wu, S.Y. Substitution of Sm^{3+} and Nd^{3+} for Bi^{3+} in $\text{SrBi}_8\text{Ti}_7\text{O}_{27}$ Mixed Aurivillius Phase. *Jpn. J. Appl. Phys. Part 1 Regul. Pap. Short Notes Rev. Pap.* **2003**, *42*, 5169. [[CrossRef](#)]
24. Lomanova, N.A. Aurivillius Phases $\text{Bi}_{m+1}\text{Fe}_{m-3}\text{Ti}_3\text{O}_{3m+3}$: Synthesis, Structure, and Properties (a Review). *Russ. J. Inorg. Chem.* **2022**, *67*, 741. [[CrossRef](#)]
25. Patri, S.K.; Choudhary, R.N.P.; Samantaray, B.K. Studies of structural; dielectric, and impedance properties of $\text{Bi}_9\text{Fe}_5\text{Ti}_3\text{O}_{27}$ ceramics. *J. Electroceram.* **2008**, *20*, 119. [[CrossRef](#)]

26. Yi, Z.G.; Li, Y.X.; Wang, Y.; Yin, Q.R. Dielectric and ferroelectric properties of intergrowth $\text{Bi}_{7-x}\text{La}_x\text{Ti}_4\text{NbO}_{21}$ ceramics. *Appl. Phys. Lett.* **2006**, *88*, 152909. [[CrossRef](#)]
27. Gao, X.; Gu, H.; Li, Y.X.; Yi, Z.G.; Čeh, M.; Žagar, K. Structural evolution of the intergrowth bismuth-layered $\text{Bi}_7\text{Ti}_4\text{NbO}_{21}$. *J. Mater. Sci.* **2011**, *46*, 5423. [[CrossRef](#)]
28. Liu, C.; Chen, Z.; Peng, R.; Fu, Z.; Zhai, X.; Lu, Y. The structure and properties of Co substituted $\text{Bi}_7\text{Ti}_4\text{NbO}_{21}$ with intergrowth phases. *RSC Adv.* **2017**, *7*, 50477. [[CrossRef](#)]
29. Giridharan, N.V.; Supriya, S. Effect of processing on the properties of $\text{Bi}_{3.15}\text{Nd}_{0.85}\text{Ti}_3\text{O}_{12}$ thin films. *Thin Solid Films* **2008**, *516*, 5244. [[CrossRef](#)]
30. Coathup, D.; Li, Z.; Zhu, X.; Yan, H.; Zhang, R.; Ye, H. Dielectric and ferroelectric properties of BTFCO thin films. *J. Electroceram.* **2019**, *43*, 92. [[CrossRef](#)]
31. Li, Y.; Li, Z.; Wang, X.; Li, H.; Su, J.; Zhang, H.; He, X.; Chi, Z.; Liu, L. Scaling behavior of dynamic hysteresis in multiferroic $\text{Bi}_5\text{FeTi}_3\text{O}_{15}$ thin films. *J. Mater. Sci. Mater. Electron.* **2021**, *32*, 27333. [[CrossRef](#)]
32. Prellier, W.; Singh, M.P.; Murugavel, P. The single-phase multiferroic oxides: From bulk to thin film. *J. Condens. Matter Phys.* **2005**, *17*, R803. [[CrossRef](#)]
33. Huang, F.; Lu, X.; Xu, T.; Liu, Y.; Su, W.; Jin, Y.; Kan, Y.; Zhu, J. Multiferroic properties of Co and Nd co-substituted $\text{Bi}_5\text{Ti}_3\text{FeO}_{15}$ thin films. *Thin Solid Films* **2012**, *520*, 6489. [[CrossRef](#)]
34. Ma, S.; Li, W.; Hao, J.; Ren, S.; Wang, M.; Xu, Z. Microstructure and ferroelectric properties of Ta-doped $\text{Bi}_{3.25}\text{La}_{0.75}\text{Ti}_3\text{O}_{12}/\text{ZnO}$ thin film capacitors. *Ceram. Int.* **2022**, *48*, 5239. [[CrossRef](#)]
35. Song, D.; Yang, J.; Yang, B.; Chen, L.; Wang, F.; Zhu, X. Evolution of structure and ferroelectricity in Aurivillius $\text{Bi}_4\text{Bi}_{n-3}\text{Fe}_{n-3}\text{Ti}_3\text{O}_{3n+3}$ thin films. *J. Mater. Chem. C* **2018**, *6*, 8618. [[CrossRef](#)]
36. Sun, H.; Lu, X.; Xu, T.; Su, J.; Jin, Y.; Ju, C.; Huang, F.; Zhu, J. Study of multiferroic properties in $\text{Bi}_5\text{Fe}_{0.5}\text{Co}_{0.5}\text{Ti}_3\text{O}_{15}$ thin films. *J. Appl. Phys.* **2012**, *111*, 124116. [[CrossRef](#)]
37. Chen, X.Q.; Yang, F.J.; Cao, W.Q.; Wang, H.; Yang, C.P.; Wang, D.Y.; Chen, K. Enhanced multiferroic characteristics in Fe-doped $\text{Bi}_4\text{Ti}_3\text{O}_{12}$ ceramics. *Solid State Commun.* **2010**, *150*, 1221. [[CrossRef](#)]
38. Chen, X.Q.; Qiao, Y.; Liu, X.L.; Lu, C.J.; Le Rhun, G.; Senz, S.; Hesse, D. Microstructure and electric properties of (104)/(014)-oriented $\text{Bi}_{3.15}\text{Nd}_{0.85}\text{Ti}_3\text{O}_{12}$ films on Pt (111)/Ti/SiO₂/Si by sol-gel method. *Mater. Lett.* **2007**, *61*, 4897. [[CrossRef](#)]
39. Sharma, N.; Kennedy, B.J.; Elcombe, M.M.; Liu, Y.; Ling, C.D. Coexistence of ferroelectricity and magnetism in transition-metal-doped $n = 3$ Aurivillius phases. *J. Condens. Matter Phys.* **2008**, *20*, 025215. [[CrossRef](#)]
40. Halpin, J.; Keeney, L. Naturally Layered Aurivillius Phases: Flexible Scaffolds for the Design of Multiferroic Materials. *OAJ Mater. Dev.* **2021**, *5*, 234. [[CrossRef](#)]
41. Joshi, P.C.; Desu, S.B. Structural and electrical characteristics of rapid thermally processed ferroelectric $\text{Bi}_4\text{Ti}_3\text{O}_{12}$ thin films prepared by metalorganic solution deposition technique. *J. Appl. Phys.* **1996**, *80*, 2349. [[CrossRef](#)]
42. Li, X.; Zhu, L.; Huang, P.; Chen, Z.; Bai, W.; Li, L.; Wen, F.; Zheng, P.; Wu, W.; Zheng, L.; et al. Reduction of oxygen vacancy concentration and large enhancement of electrical performances in Cu/Sb co-doped $\text{Bi}_4\text{Ti}_3\text{O}_{12}$ high-temperature piezoelectric ceramics. *J. Appl. Phys.* **2020**, *127*, 044102. [[CrossRef](#)]
43. Bokolia, R.; Thakur, O.P.; Rai, V.K.; Sharma, S.K.; Sreenivas, K. Electrical properties and light upconversion effects in $\text{Bi}_{3.79}\text{Er}_{0.03}\text{Yb}_{0.18}\text{Ti}_{3-x}\text{W}_x\text{O}_{12}$ ferroelectric ceramics. *Ceram. Int.* **2016**, *42*, 5718. [[CrossRef](#)]
44. Stojanović, B.D.; Paiva-Santos, C.O.; Cilense, M.; Jovalekić, Č.; Lazarević, Z.Ž. Structure study of $\text{Bi}_4\text{Ti}_3\text{O}_{12}$ produced via mechanochemically assisted synthesis. *Mater. Res. Bull.* **2008**, *43*, 1743. [[CrossRef](#)]
45. Prasad, N.V.; Prasad, G.; Kumar, G.S.; Karmakar, S.; Gupta, S.M. Electrical relaxation studies on lanthanum and vanadium modified $\text{Bi}_4\text{Ti}_3\text{O}_{12}$. *Ferroelectrics* **2012**, *437*, 88. [[CrossRef](#)]
46. Lavado, C.; Stachiotti, M.G. $\text{Fe}^{3+}/\text{Nb}^{5+}$ co-doping effects on the properties of Aurivillius $\text{Bi}_4\text{Ti}_3\text{O}_{12}$ ceramics. *J. Alloys Compd.* **2018**, *731*, 914. [[CrossRef](#)]
47. Wang, W.; Shen, X.; Wang, W.; Guan, X.; Yao, Y.; Wang, Y.; Yu, R. The Evolution of Microstructure and Magnetic Properties of the Bismuth Layer Compounds with Cobalt Ions Substitution. *Inorg. Chem.* **2017**, *56*, 3207. [[CrossRef](#)]
48. Ferreira, W.C.; Rodrigues, G.L.C.; Araújo, B.S.; de Aguiar, F.A.A.; de Abreu Silva, A.N.A.; Fachine, P.B.A.; de Araujo Paschoal, C.W.; Ayala, A.P. Pressure-induced structural phase transitions in the multiferroic four-layer Aurivillius ceramic $\text{Bi}_5\text{FeTi}_3\text{O}_{15}$. *Ceram. Int.* **2020**, *46*, 18056. [[CrossRef](#)]
49. Shigyo, T.; Kiyono, H.; Nakano, J.; Itoh, H.; Takahashi, J. Synthesis and dielectric-magnetic properties of rare-earth (La, Nd, Sm)-modified $\text{Bi}_4\text{Ti}_3\text{O}_{12}$. *Jpn. J. Appl. Phys.* **2008**, *47*, 7617. [[CrossRef](#)]
50. Paul, J.; Bhardwaj, S.; Sharma, K.K.; Kotnala, R.K.; Kumar, R. Room-temperature multiferroic properties and magnetoelectric coupling in $\text{Bi}_{4-x}\text{Sm}_x\text{Ti}_{3-x}\text{Co}_x\text{O}_{12-\delta}$ ceramics. *J. Mater. Sci.* **2014**, *49*, 6056. [[CrossRef](#)]
51. Yu, Z.; Meng, X.; Zheng, Z.; Lu, Y.; Chen, H.; Huang, C.; Sun, H.; Liang, K.; Ma, Z.; Qi, Y.; et al. Room temperature multiferroic properties of rare-earth-substituted Aurivillius phase $\text{Bi}_5\text{Ti}_3\text{Fe}_{0.7}\text{Co}_{0.3}\text{O}_{15}$ ceramics. *Mater. Res. Bull.* **2019**, *115*, 235. [[CrossRef](#)]
52. Chakrabarti, A.; Bera, J. Effect of La-substitution on the structure and dielectric properties of $\text{BaBi}_4\text{Ti}_4\text{O}_{15}$ ceramics. *J. Alloys Compd.* **2010**, *505*, 668. [[CrossRef](#)]
53. Patri, T.; Kumar, J.P.; Ghosh, A.; Babu, P.D. Tunable polarization with enhanced multiferroic response of W/Co co-doped $\text{Bi}_4\text{LaFeTi}_3\text{O}_{15}$ Aurivillius ceramics. *J. Appl. Phys.* **2020**, *128*, 154102. [[CrossRef](#)]

54. Algueró, M.; Pérez-Cerdán, M.; del Real, R.P.; Ricote, J.; Castro, A. Novel Aurivillius $\text{Bi}_4\text{Ti}_{3-2x}\text{Nb}_x\text{Fe}_x\text{O}_{12}$ phases with increasing magnetic-cation fraction until percolation: A novel approach for room temperature multiferroism. *J. Mater. Chem. C* **2020**, *8*, 12457. [[CrossRef](#)]
55. Mandal, T.K.; Sivakumar, T.; Augustine, S.; Gopalakrishnan, J. Heterovalent cation-substituted Aurivillius phases, $\text{Bi}_2\text{SrNaNb}_2\text{TaO}_{12}$ and $\text{Bi}_2\text{Sr}_2\text{Nb}_{3-x}\text{M}_x\text{O}_{12}$ ($\text{M} = \text{Zr}, \text{Hf}, \text{Fe}, \text{Zn}$). *Mater. Sci. Eng. B* **2005**, *121*, 112. [[CrossRef](#)]
56. Yu, W.J.; Kim, Y.I.; Ha, D.H.; Lee, J.H.; Park, Y.K.; Seong, S.; Hur, N.H. A new manganese oxide with the Aurivillius structure: $\text{Bi}_2\text{Sr}_2\text{Nb}_2\text{MnO}_{12-\delta}$. *Solid State Commun.* **1999**, *111*, 705. [[CrossRef](#)]
57. Veenachary, V.; Ramana, E.V.; Babu, S.N.; Puli, V.S.; Srinivas, A.; Srinivasan, G.; Saha, S.; Prasad, G.; Prasad, N.V. Magnetic and Magnetoelectric Properties of Aurivillius Three- and Four-Layered Intergrowth Ceramics. *Crystals* **2023**, *13*, 426. [[CrossRef](#)]
58. Ramana, E.V.; Prasad, N.V.; Tobaldi, D.M.; Zavašnik, J.; Singh, M.K.; Hortigüela, M.J.; Seabra, M.P.; Prasad, G.; Valente, M.A. Effect of samarium and vanadium co-doping on structure, ferroelectric and photocatalytic properties of bismuth titanate. *RSC Adv.* **2017**, *7*, 9680. [[CrossRef](#)]
59. Hume-Rothery, R. *Van Nostrand's Scientific Encyclopaedia*; John Wiley & Sons, Inc.: New York, NY, USA, 2002.
60. Suárez, D.Y.; Reaney, I.M.; Lee, W.E. Relation between tolerance factor and T_c in Aurivillius compounds. *J. Mater. Res.* **2001**, *16*, 3139. [[CrossRef](#)]
61. Zhang, D.L.; Huang, W.C.; Chen, Z.W.; Zhao, W.B.; Feng, L.; Li, M.; Yin, Y.W.; Dong, S.N.; Li, X.G. Structure evolution and multiferroic properties in cobalt doped $\text{Bi}_4\text{NdTi}_3\text{Fe}_{1-x}\text{Co}_x\text{O}_{15}$ - $\text{Bi}_3\text{NdTi}_2\text{Fe}_{1-x}\text{Co}_x\text{O}_{12-\delta}$ Intergrowth Aurivillius Compounds. *Sci. Rep.* **2017**, *7*, 43540. [[CrossRef](#)] [[PubMed](#)]
62. Das, S.R.; Dabal, P.S.; Sundarakannan, B.; Das, R.R.; Katiyar, R.S. Micro-Raman study of Zr-substituted $\text{Bi}_4\text{Ti}_3\text{O}_{12}$ ceramics. *J. Raman Spectrosc.* **2007**, *38*, 1077. [[CrossRef](#)]
63. Wu, D.; Deng, Y.; Mak, C.L.; Wong, K.H.; Li, A.D.; Zhang, M.S.; Ming, N.B. Raman scattering study of La-, Nd- And Sm-substituted $\text{Bi}_4\text{Ti}_3\text{O}_{12}$. *Appl. Phys. A Mater. Sci. Process.* **2005**, *80*, 607. [[CrossRef](#)]
64. Ti, R.; Lu, X.; He, J.; Huang, F.; Wu, H.; Mei, F.; Zhou, M.; Li, Y.; Xu, T.; Zhu, J. Multiferroic properties and magnetoelectric coupling in Fe/Co co-doped $\text{Bi}_{3.25}\text{La}_{0.75}\text{Ti}_3\text{O}_{12}$ ceramics. *J. Mater. Chem. C* **2015**, *3*, 11868. [[CrossRef](#)]
65. Ramana, E.V.; Figueiras, F.; Mahajan, A.; Tobaldi, D.; Costa, B.F.O.; Graça, M.P.F.; Valente, M.A. Effect of Fe-doping on the structure and magnetoelectric properties of $(\text{Ba}_{0.85}\text{Ca}_{0.15})(\text{Ti}_{0.9}\text{Zr}_{0.1})\text{O}_3$ synthesized by a chemical route. *J. Mater. Chem. C* **2016**, *4*, 1066. [[CrossRef](#)]
66. Yin, Z.; Sheng, Y.; Ma, G. Dielectric, multiferroic and magnetodielectric properties of Co/Fe co-doped $\text{Bi}_4\text{Ti}_3\text{O}_{12}$ ceramics. *J. Mater. Sci. Mater. Electron.* **2019**, *30*, 10483. [[CrossRef](#)]
67. Long, C.; Ren, W.; Li, Y.; Liu, L.; Xia, Y.; Fan, H. High oxide ion conductivity in layer-structured $\text{Bi}_4\text{Ti}_3\text{O}_{12}$ -based ferroelectric ceramics. *J. Mater. Chem. C* **2019**, *7*, 8825. [[CrossRef](#)]
68. Kumar, J.P.; Sekhar, K.S.K.R.C.; Rao, T.D.; Babu, P.D.; Tirupathi, P. Effect of sintering temperature on structural, dielectric, and electrical property studies of $\text{Bi}_4\text{NdTi}_3\text{FeO}_{15}$ Aurivillius ceramics. *J. Mater. Sci. Mater. Electron.* **2021**, *32*, 9675. [[CrossRef](#)]
69. Goodenough, J.B. Electronic and ionic transport properties and other physical aspects of perovskites. *Rep. Prog. Phys.* **2004**, *67*, 1915. [[CrossRef](#)]
70. Shet, T.; Bhimireddi, R.; Varma, K.B.R. Grain size-dependent dielectric, piezoelectric and ferroelectric properties of $\text{Sr}_2\text{Bi}_4\text{Ti}_5\text{O}_{18}$ ceramics. *J. Mater. Sci.* **2016**, *51*, 9253. [[CrossRef](#)]
71. Kumar, S.; Varma, K.B.R. Dielectric relaxation in bismuth layer structured $\text{BaBi}_4\text{Ti}_4\text{O}_{15}$ ferroelectric ceramics. *Curr. Appl. Phys.* **2011**, *11*, 203. [[CrossRef](#)]
72. Mohapatra, S.R.; Sahu, B.; Badapanda, T.; Pattanaik, M.S.; Kaushik, S.D.; Singh, A.K. Optical, dielectric relaxation and conduction study of $\text{Bi}_2\text{Fe}_4\text{O}_9$ ceramic. *J. Mater. Sci. Mater. Electron.* **2016**, *27*, 3645. [[CrossRef](#)]
73. Patri, T.; Ghosh, A.; Mahesh, M.L.V.; Babu, P.D.; Mandal, S.K.; Singh, M.N. Fortified relaxor ferroelectricity of rare earth substituted 4-layered $\text{BaBi}_{3.9}\text{RE}_{0.1}\text{Ti}_4\text{O}_{15}$ ($\text{RE} = \text{La}, \text{Pr}, \text{Nd}, \text{and Sm}$) Aurivillius compounds. *Sci. Rep.* **2022**, *12*, 16508. [[CrossRef](#)]
74. Zhang, H.; Yan, H.; Ning, H.; Reece, M.J.; Eriksson, M.; Shen, Z.; Kan, Y.; Wang, P. The grain size effect on the properties of Aurivillius phase $\text{Bi}_{3.15}\text{Nd}_{0.85}\text{Ti}_3\text{O}_{12}$ Ferroelectric ceramics. *Nanotechnology* **2009**, *20*, 385708. [[CrossRef](#)]
75. Nayak, P.; Badapanda, T.; Singh, A.K.; Panigrahi, S. Possible relaxation and conduction mechanism in W^{6+} -doped $\text{SrBi}_4\text{Ti}_4\text{O}_{15}$ ceramic. *Ceram Int.* **2017**, *43*, 4527. [[CrossRef](#)]
76. Rehman, F.; Li, J.B.; Dou, Y.K.; Zhang, J.S.; Zhao, Y.J.; Rizwan, M.; Khalid, S.; Jin, H.B. Dielectric relaxations and electrical properties of Aurivillius $\text{Bi}_{3.5}\text{La}_{0.5}\text{Ti}_2\text{Fe}_{0.5}\text{Nb}_{0.5}\text{O}_{12}$ ceramics. *J. Alloys Compd.* **2016**, *654*, 315. [[CrossRef](#)]
77. Thomas, A.K.; Abraham, K.; Thomas, J.; Saban, K.V. Electrical and dielectric behaviour of $\text{Na}_{0.5}\text{La}_{0.25}\text{Sm}_{0.25}\text{Cu}_3\text{Ti}_4\text{O}_{12}$ ceramics investigated by impedance and modulus spectroscopy. *J. Asian Ceram. Soc.* **2017**, *5*, 56. [[CrossRef](#)]
78. Rehman, F.; Li, J.B.; Ahmed, P.; Khan, M.S.; Saeed, Y.; Khan, A.; Zubair, M. Dielectric relaxation and conduction behaviors of Aurivillius $\text{Na}_{0.5}\text{Bi}_{4.5}\text{Ti}_4\text{O}_{15}$ ceramics with Na doping. *Rare Metals* **2021**, *40*, 1247. [[CrossRef](#)]
79. Ramana, E.V.; Prasad, N.V.; Figueiras, F.; Lajaunie, L.; Arenal, R.; Otero-Irurueta, G.; Valente, M.A. The growth and improved magnetoelectric response of strain modified Aurivillius $\text{SrBi}_{4.25}\text{La}_{0.75}\text{Ti}_4\text{FeO}_{18}$ thin films. *Dalton Trans.* **2019**, *48*, 13224. [[CrossRef](#)] [[PubMed](#)]
80. Faraz, A.; Maity, T.; Schmidt, M.; Deepak, N.; Roy, S.; Pemble, M.E.; Whatmore, R.W.; Keeney, L. Direct visualization of magnetic-field-induced magnetoelectric switching in multiferroic Aurivillius phase thin films. *J. Am. Ceram. Soc.* **2017**, *100*, 975. [[CrossRef](#)]

81. Paul, J.; Bhardwaj, S.; Sharma, K.K.; Kotnala, R.K.; Kumar, R. Room temperature multiferroic properties and magnetoelectric coupling in Sm and Ni substituted $\text{Bi}_{4-x}\text{Sm}_x\text{Ti}_{3-x}\text{Ni}_x\text{O}_{12\pm\delta}$ ($x = 0, 0.02, 0.05, 0.07$) ceramics. *J. Appl. Phys.* **2014**, *115*, 204909. [[CrossRef](#)]
82. Zhao, H.; Kimura, H.; Cheng, Z.; Osada, M.; Wang, J.; Wang, X.; Dou, S.; Liu, Y.; Yu, J.; Matsumoto, T.; et al. Large magnetoelectric coupling in magnetically short-range ordered $\text{Bi}_5\text{Ti}_3\text{FeO}_{15}$ film. *Sci. Rep.* **2014**, *4*, 5255. [[CrossRef](#)]
83. Ramana, E.V.; Mahajan, A.; Graça, M.P.F.; Srinivas, A.; Valente, M.A. Ferroelectric and magnetic properties of magnetoelectric $(\text{Na}_{0.5}\text{Bi}_{0.5})\text{TiO}_3\text{-BiFeO}_3$ synthesized by acetic acid assisted sol-gel method. *J. Eur. Ceram. Soc.* **2014**, *34*, 4201. [[CrossRef](#)]
84. Ti, R.; Wang, C.; Wu, H.; Xu, Y.; Zhang, C. Study on the structural and magnetic properties of Fe/Co co-doped $\text{Bi}_4\text{Ti}_3\text{O}_{12}$ ceramics. *Ceram. Int.* **2019**, *45*, 7480–7487. [[CrossRef](#)]
85. Wang, Y.; Wang, H.; Tan, W.; Huo, D. Magnetization reversal; critical behavior, and magnetocaloric effect in NdMnO_3 : The role of magnetic ordering of Nd and Mn moments. *J. Appl. Phys.* **2022**, *132*, 183907. [[CrossRef](#)]
86. Bai, W.; Chen, C.; Yang, J.; Zhang, Y.; Qi, R.; Huang, R.; Tang, X.; Duan, C.G.; Chu, J. Dielectric behaviors of Aurivillius $\text{Bi}_5\text{Ti}_3\text{Fe}_{0.5}\text{Cr}_{0.5}\text{O}_{15}$ multiferroic polycrystals: Determining the intrinsic magnetoelectric responses by impedance spectroscopy. *Sci. Rep.* **2015**, *5*, 17846. [[CrossRef](#)] [[PubMed](#)]
87. Li, T.; Wang, H.; Ma, D.; Li, K.; Hu, Z. Influence of clamping effect in BaTiO_3 film on the magnetoelectric behavior of layered multiferroic heterostructures. *Mater. Res. Bull.* **2019**, *115*, 116. [[CrossRef](#)]
88. Liu, Y.; Pu, Y.; Sun, Z. Correlation between lattice distortion and magnetic and electrical properties of Fe-doped $\text{Bi}_4\text{Ti}_3\text{O}_{12}$ ceramics. *J. Mater. Sci. Mater. Electron.* **2015**, *26*, 7484. [[CrossRef](#)]

Disclaimer/Publisher’s Note: The statements, opinions and data contained in all publications are solely those of the individual author(s) and contributor(s) and not of MDPI and/or the editor(s). MDPI and/or the editor(s) disclaim responsibility for any injury to people or property resulting from any ideas, methods, instructions or products referred to in the content.